Forces Acting in Flowing Beds of Solids

JOHN W. DELAPLAINE
University of Delaware, Newark, Delaware

Beds of granular solids flowing downward under the influence of gravity as a consolidated or dense phase have found wide application in recent years as media for effecting chemical and physical changes. Typical applications of the so-called "moving-bed" principle are the Houdriflow and TCC catalytic cracking units and the pebble heater. This technique provides a method for carrying out concurrent or countercurrent operations under controlled temperature gradients and has numerous applications in the chemical field.

This paper presents the results of a study of the stresses acting in beds of noncohesive granular solids flowing under steady state conditions in vertical vessels of constant cross section with no interstitial fluid flow relative to the solids. It is important to examine this relatively simple case of solids flow, which is of industrial significance, before systems involving solids acceleration and fluid pressure gradient can be effectively analyzed. The objectives of this study are to determine as many as possible of the fundamental laws governing solids flow by investigating the stress relationships and to explain the characteristics of flowing beds of solids.

The behavior of both static- and flowing-solids systems differs from that of comparable fluid systems. Solids systems have a finite angle of repose and the mechanism of stress distribution is by particle-to-particle friction. The stresses, or forces per unit area, are exerted by the particles on each other (local or internal stresses) and at the boundaries of the bed (boundary or wall stresses). Numerous investigators (*6, 7, 9, 16*) have measured the boundary forces exerted by static beds of solids. They have shown that the stresses are not proportional to the bed depth but increase exponentially until asymptotic values are reached at bed-depth–to-tube-diameter ratios of about 5. In a flowing consolidated bed of Ottawa sand particles Brinn et al. (*3*) have shown that the velocity over approximately the central 80% of the bed was constant and the flow in this region was rodlike. Shear occurred in the outer region of the bed, and the velocity at the walls was found to be slightly lower than the average. This report will discuss how and why solids systems behave differently from fluids. It will also extend stress-relationship data from boundary stresses in static systems to both local and boundary stresses in flowing systems.

Present address: Cox and Weinrich, Washington, D. C.

STRESS THEORY AND LITERATURE SURVEY

Equations of continuity of momentum are needed for the stress relationships in flowing beds of solids. The local stresses are related by balances around a differential volume of solids, $r\,dr\,d\theta\,dz$, shown in Figure 1, and the boundary and average stresses by a balance around a horizontal slab of $(\pi D_t^2/4)\,dz$ volume. Moment balances are used to simplify the local stress equations, and stress ratios are introduced to simplify both types of equations. Experimental data will be utilized to evaluate these stress ratios and the basic equations, so that all stresses may be calculated as functions of fractional radius, bed depth, pipe diameter, bulk density, and friction coefficients. Throughout this paper the buoyancy and local gravitational effects have been included in the term ρ_b for simplification, so that ρ_b represents a net force per unit volume of solids rather than a solids density.

Forces Acting on a Differential Volume

Figure 1 shows the stresses acting on an infinitesimally small volume in cylindrical coordinates, along with the areas on which these stresses act. There are three normal (compressive) stresses, σ_r, σ_θ, and σ_z, resulting from forces in the r, θ, and z directions acting on perpendicular planes. There are six shear stresses, τ_{zr}, τ_{rz}, $\tau_{\theta z}$, $\tau_{z\theta}$, $\tau_{\theta r}$, and $\tau_{r\theta}$, acting parallel to the plane of the stress in the direction of the second subscript and resulting from a normal force in the direction of the first subscript. If acceleration is absent and gravity is the only body force, the equations for these stresses are as follows, the downward, radial, and clockwise directions being taken as positive:

$$\frac{\partial \sigma_z}{\partial z} + \frac{\partial \tau_{rz}}{\partial r} + \frac{\partial \tau_{\theta z}}{r\,\partial \theta} + \frac{\tau_{rz}}{r} = \rho_b \quad (1)$$

$$\frac{\partial \sigma_r}{\partial r} + \frac{\partial \tau_{zr}}{\partial z} + \frac{\partial \tau_{\theta r}}{r\,\partial \theta} + \frac{\sigma_r - \sigma_\theta}{r} = 0 \quad (2)$$

$$\frac{\partial \sigma_\theta}{r\,\partial \theta} + \frac{\partial \tau_{z\theta}}{\partial z} + \frac{\partial \tau_{r\theta}}{\partial r} + \frac{\tau_{\theta r} + \tau_{r\theta}}{r} = 0 \quad (3)$$

These equations were obtained by direct substitution of the body forces in the classical equations for static equilibrium under nonuniform stress conditions given by Sechler (*12*), Westergaard (*17*), and others. If angular acceleration is absent, these authors show that moment balances around the radial, vertical, and tangential axes yield $\tau_{\theta z} = \tau_{z\theta}$, $\tau_{r\theta} = \tau_{\theta r}$, and $\tau_{rz} = \tau_{zr}$. For example, in the upper right-hand corner of Figure 1 the shear stresses $\tau_{r\theta}$ and $\tau_{\theta r}$ acting on the small square of the differential section must be equal and must give rise to opposite moments, or the particles will rotate around the vertical axis. If acceleration exists, the resultant force or moment from Newton's second law must be included in the appropriate equation.

Jaky (*5*) in a purely mathematical analysis of a static system of solids used two-dimensional stress differential equations. However, his final equations do not appear to be valid because of the numerous assumptions, such as the proportionality of both the shear stress and the coefficient of friction with bed depth.

The stress ratios used to simplify the force-balance equations for a differential volume are defined in the following table together with the ratios for a horizontal slab.

Table 1

Local stress ratios, differential volume	Boundary and average stress ratios, horizontal slab
$\mu = \dfrac{\tau_{rz}}{\sigma_r}$	$\mu' = \dfrac{(\tau_{rz})_w}{(\sigma_r)_w}$ = friction coefficient
$k = \dfrac{\sigma_r}{\sigma_z}$	$k_a = \dfrac{(\sigma_r)_w}{(\sigma_z)_a}$
	$\alpha = \dfrac{(\sigma_z)_a}{4(\tau_{rz})_w} = \dfrac{1}{4k_a\mu}$

where the subscript w refers to the boundary or wall stress and $(\sigma_z)_a$ is the average vertical stress (i.e., total vertical force on a horizontal plane divided by its area). These ratios vary with the stress, bed depth, and radial distance.

Forces Acting on a Horizontal Slab

Figure 2a shows the boundary and average forces acting on a horizontal slab of solids within the bed. A vertical force balance on this horizontal slab of solids of thickness dz gives

$$\frac{d(\sigma_z)_a}{dz} = \rho_b - \frac{4(\tau_{rz})_w}{D_t} \tag{4}$$

Substitution of the stress ratios yields

$$\frac{d(\sigma_z)_a}{dz} = \rho_b - \frac{4k_a\mu'(\sigma_z)_a}{D_t}$$

$$= \rho_b - \frac{(\sigma_z)_a}{\alpha D_t} \tag{5}$$

The classical solution to this equation was given by Janssen (*6*), who assumed k_a, μ', and α to be independent of bed depth and integrated from 0 to z bed depth. Thus

$$(\sigma_z)_a = \frac{\rho_b D_t}{4k_a\mu'}\left(1 - e^{-4k_a\mu' z/D_t}\right)$$

$$= \alpha\rho_b D_t[1 - e^{-z/(\alpha D_t)}] \tag{6}$$

Several investigators (*6, 7, 9, 16*) have found that at bed depths of less than about five tube diameters the stresses vary with bed depth, and at z/D_t ratios greater than about 5, stresses are independent of z. The bed therefore may be considered to be composed of these two sections. The subscript h will be used to refer to values of stress at high bed depths ($z/D_t > 5$). Figure 2b shows these stresses. In this region $d(\sigma_z)_{a,h}/dz = 0$; all the additional weight of solids is supported by the tube wall, and Equations (5) and (4) reduce to

$$\frac{(\sigma_z)_{a,h}}{\rho_b D_t} = \frac{1}{4k_{a,h}\mu_h'} = \alpha_h \tag{7}$$

and

$$\frac{(\tau_{rz})_{w,h}}{\rho_b D_t/4} = \frac{(\sigma_z)_{a,h}}{\alpha_h \rho_b D_t} = 1 \tag{8}$$

where α_h, $k_{a,h}$ and μ_h' are the stress ratios existing at high bed depths. Equation (7) shows that the maximum vertical force in a bed of solids equals its weight within the height αD_t. Equation (6) gives satisfactory values at relatively high bed depths if α or $k_a\mu'$ is measured at high bed depths.

Investigations of solids stresses have been limited essentially to boundary measurements in static systems. Most investigators (*7, 9, 16*) have correlated their stress measurements by the Janssen equation (5) using a constant value of k_a equal to the ratio of radial to horizontal stress in an unconfined bed of solids, which is a function of the coefficient of friction between particles. However, the available experimental data do not indicate that these assumptions are correct. Shaxby and Evans (*14*) developed a different equation for stress exerted by static powders, but a differentiation of their basic equation indicates that the slope of their $(\sigma_z)_a$-vs.-z curve at low bed depths differs by several hundred per cent from the solids density. These must be equal, as will be shown later. Caquot and Karisel (*4*) present an empirical equation for the variation of vertical stress with bed depth which involves an unknown constant. Since data are not available, they suggest that this constant is zero, and their equation reduces to the conventional Janssen equation (5).

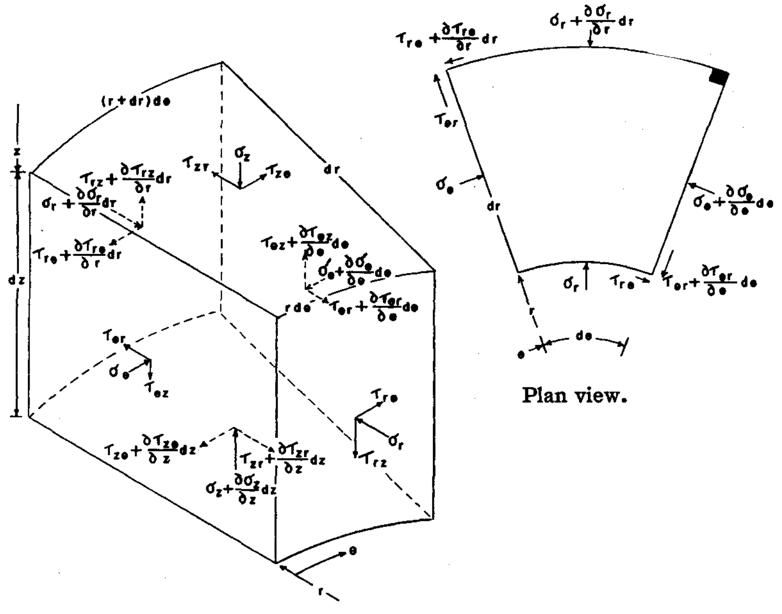

Fig. 1. Forces acting on a differential volume in cylindrical coordinates.

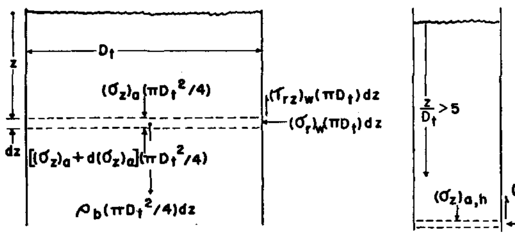

a b

Fig. 2. Boundary and average stresses: a, force balance; b, stresses at high bed depth.

SCOPE OF WORK

In the previous section it was indicated that the basic differential equations for static systems are known but that satisfactory integrations have not been obtained. The present investigation is concerned with the determination of the stresses and evaluation of these equations in flowing-solids systems. The boundary stresses $(\sigma_r)_w$ and $(\tau_{rz})_w$, the average vertical stress $(\sigma_z)_a$, and the local stresses σ_z, σ_r, and σ_θ were measured, and the remaining shear stresses were calculated from the theoretical equations developed. In addition, the required solids properties, density and friction coefficients, were determined. The relationships between the boundary and average stresses were developed from a force balance on a differential slab of solids. The relationships of the local stresses were determined from balances on a differential volume of solids.

To make the final correlations as general as possible, the tube-to-particle-diameter ratio was varied from about 10/1 to 400/1 and different solids materials were investigated. Runs were made in the following containers: (1) smooth steel tubing from 0.5 to 3.806 in. in diameter, (2) commercial (rusty) pipe 4.026 and 11.63 in. in diameter, and (3) a 5-ft.-diam. brick-lined vessel. The particle diameter varied from 0.009 to 0.14 in. The materials studied were spherical glass beads, ellipsoidal bead catalyst, and irregularly shaped, rounded Ottawa test sand particles. Their properties are listed in Table 2.

TABLE 2. DENSITY DATA

Material	Mesh	D_p, in.	ρ_p, g./cu. in.	ρ_b, g./cu. in. (flowing)
Sand	20–30	0.029	43.6	25.7
	30–36	0.022	43.6	25.1
	36–48	0.015	43.6	24.85
	48–55	0.012	43.6	24.35
	50–70	0.009	43.6	23.9
Glass beads	25–30	0.028	40.7	24.95
	35–40	0.0185	40.9	24.8
	50–60	0.011	42.5	25.7
Bead catalyst	3–10	0.125	19.3	12.1

EXPERIMENTAL METHODS

Apparatus

The equipment consisted of the system being studied, the pick-up gauge, the force transmission device, and the measuring circuit. The gauges and measurements will be discussed later in this section. Figure 3 is a photograph of the 3.80-in.-diameter apparatus which was similar to the other systems investigated. This picture shows the 6-ft. length of tubing, feed funnel, traversing mechanisms, and wall-forces gauge. A four-holed orifice located below the tubing maintained constant solids flow rate. This multi-holed orifice minimized the bed depth required to eliminate the effect of the orifice on the stresses by considerably reducing the height of stagnant solids below the height required above a single orifice.

The accurate transmission of each type of stress to the point of measurement required an instrument development program. The effect on the measurements of any stationary equipment in the bed had to be determined. It was necessary to hold the volume of any stationary internal device to a minimum. The internal stress measurements were made by hanging the plate or cylinder from a Statham transducer with 0.010-in.-diam. stainless hypodermic tubing, surrounded by a slightly larger stationary hypodermic shield to eliminate shear stress on the inner tube. The effect of the support tubing, shield, and thin alignment rods on the results was determined experimentally to be negligible.

In general, loads were measured with the Statham transducer, which contains a Wheatstone bridge the resistances of which vary with the load. This instrument was chosen because of its negligible deformation, linearity, sensitivity, and ease of calibration. A direct-current input was used and the output was recorded on a strip-chart self-balancing potentiometer. Direct calibrations with known weights were made after all runs.

Procedures

The variable in each run was bed depth. The system was "prerun" by allowing it to flow for a period of 10 min. to establish equilibrium stress conditions, and the level fell when feeding ceased at the beginning of the test period. It was necessary continually to level the top of the bed by hand during the run because of the lower velocity near the wall. The level varied linearly with time, an indication of constant density and velocity.

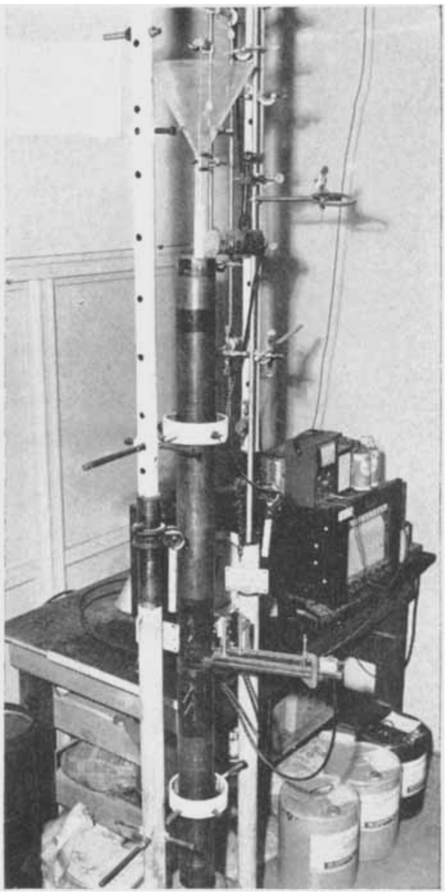

Fig. 3. Equipment.

Wall-forces-gauge Measurements

This gauge, shown in Figure 4, simultaneously measured $(\tau_{rz})_w$ and $(\sigma_r)_w$ and μ', which equals $(\tau_{rz})_w/(\sigma_r)_w$. The horizontal force on a 1.245-in.-diam. curved disk in a 1.25-in. hole was transmitted through a pivoted shaft to a transducer. This shaft was supported by a spring steel strip from a vertical transducer, which measured the moment of the $(\tau_{rz})_w$ force about the pivot. This moment balance was verified by hanging weights from the disk surface. The reading of each transducer was unaffected by mechanical forces on the disk in the perpendicular direction.

The measured vertical load divided by the elliptical surface area equaled $(\tau_{rz})_w$. However, at low bed depths the center of radial pressure was below the disk centroid. This radial moment necessitated a small correction to $(\tau_{rz})_w$. The measured horizontal load divided by the projection of the area on a tangential plane (circle) equaled $(\sigma_r)_w$. The bed depth corresponding to the measurements was approximately equal to the distance from the free surface to the centroid of the disk. At low bed depths, only the disk area covered by solids is pertinent.

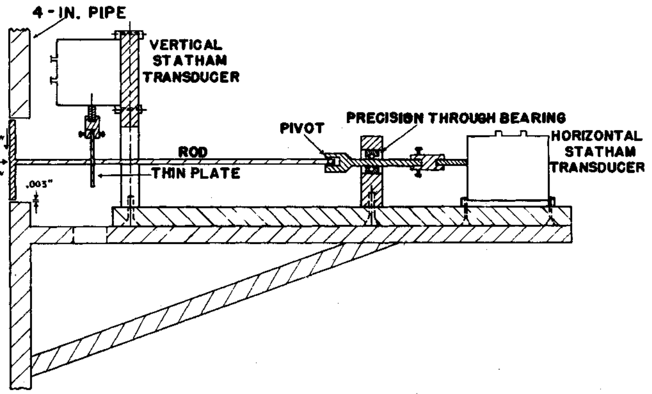

Fig. 4. Wall-forces gauge; 1.25-in.-diam. diaphragm forms extension of inner surface of 4-in. pipe.

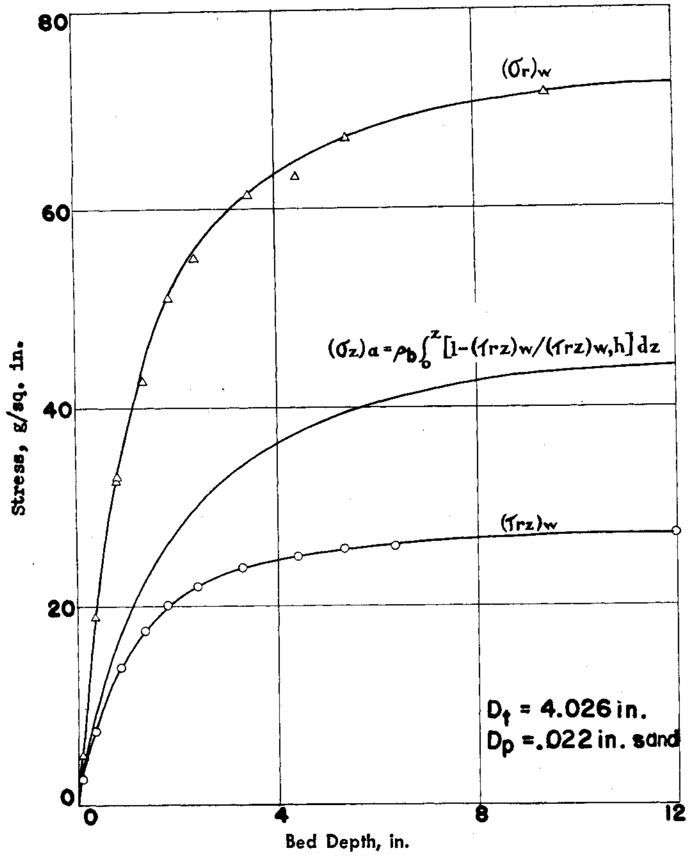

Fig. 5. Wall-forces-gauge measurements.

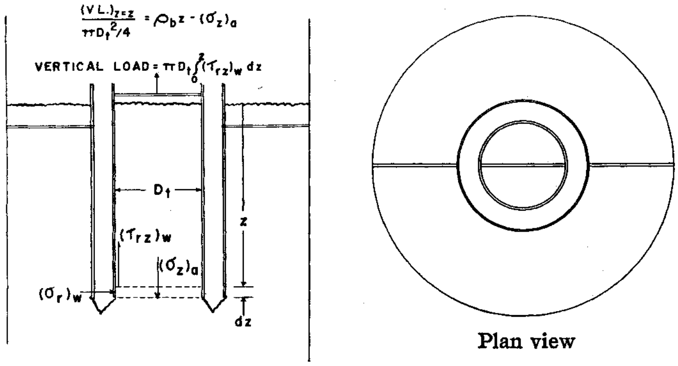

Fig. 6. Total-load measurements.

The validity of the measurements is demonstrated by the equality of the measured values of $(\tau_{rz})_{w,h}$ and the expected value from Equation (8) of $\rho_b D_t/4$. The average vertical stress at any bed depth was calculated from Equations (4) and (8) by graphical integration. Thus

$$(\sigma_z)_a = \rho_b \int_0^z \left[1 - \frac{(\tau_{rz})_w}{(\tau_{rz})_{w,h}}\right] dz \quad (9)$$

The stress ratios k_a, μ', and α were calculated at various bed depths from these stresses by the equations given in Table 1 and from Equations (7) and (8) at high bed depths. All stresses were found to be zero at zero bed depth. However, the limiting stress ratios at zero bed depth can be calculated by L'Hôpital's rule from the initial slopes of the appropriate stress-vs.-bed-depth curves. At zero bed depth (subscript 0), $(\sigma_z)_{a,0}$ equals zero, and from Equation (5)

$$\left[\frac{d(\sigma_z)_a}{\rho_b\, dz}\right]_0 = 1 \quad (10)$$

From Equation (10) and Table 1

$$k_{a,0} = \left[\frac{d(\sigma_r)_w}{\rho_b\, dz}\right]_0$$

$$\alpha_0 = \frac{1/4}{\left[\frac{d(\tau_{rz})_w}{\rho_b\, dz}\right]_0} \quad (11)$$

$$\mu_0' = \frac{\left[\frac{d(\tau_{rz})_w}{\rho_b\, dz}\right]_0}{\left[\frac{d(\sigma_r)_w}{\rho_b\, dz}\right]_0}$$

Figure 5 is a plot of the data from a typical wall-forces-gauge experiment.

Total-load Measurements

The vertical load, or total wall shear force $(\pi D_t) \int_0^z (\tau_{rz})_w\, dz$, was measured by suspending the tubing from a transducer, and $(\tau_{rz})_w$ was calculated from the slope of the load-vs.-bed-depth curve divided by πD_t. The most satisfactory results were obtained with the concentric-cylinder apparatus shown in Figure 6, along with the pertinent stresses on a controlled volume of solids. The solids velocity was controlled with the multiholed orifice located several feet below the cylinders. The annular space between the cylinders contained no solids, and so shear only from within the inner tube was measured. To calibrate the concentric-cylinder apparatus, similar experiments were carried out with both cylinders full. The limitation of these experiments is that $(\sigma_r)_w$ must be calculated as $(\tau_{rz})_w/\mu'$. The friction coefficient from wall-forces-gauge measurements was used.

From a force balance on the solids within the volume $(\pi D_t^2/4)z$,

$$(\sigma_z)_a = \rho_b z - \text{vert. load}/(\pi D_t^2/4)$$

Table 1 gives the equations for α and k_a. The validity of the method is demonstrated by the comparison in Figure 7 of $(\tau_{rz})_{w,h}/(\rho_b D_t/4)$ and $[d(\sigma_z)_a/\rho_b dz]_0$ with their expected value of 1.0 from Equations (8) and (10). Figure 7 is a plot of the data from a typical total-load experiment.

Average-vertical-stress Measurements

A grid of thin, perpendicular, vertical plates 2 ft. high with 6-in.-square openings and an effective cross section of (0.785) $(4.65)^2$ = 17 sq. ft. was suspended in a 5-ft.-diam. brick-lined vessel. The effective area was less than the total because the brick wall surrounding the grid carried part of the vertical force. Strain gauges were attached to the support rods and to a dummy rod. This method measures $(\sigma_z)_a$ by allowing all the vertical force across a horizontal plane to be exerted as shear on the grid except that transmitted by the solids flowing past the grid.

Figure 8*a* and *b*, for zero and finite bed depths above the top of the grid, shows the vertical force balances on the solids within the volumes $(\pi D_e^2/4)L$ and the stresses on a controlled volume within one of the grid openings. The experimental data indicate that at appreciable bed depths above an internal tube the stress ratio k_a within the tube has already attained its maximum (asymptotic) value. Therefore, in Figure 8*b*, k_a and α_g are constant at values of $k_{a,h}$ and $\alpha_{g,h}$ and Equation (5) can be integrated from M, where $(\sigma_z)_a = (\sigma_z)_{a,t}$, to N to give at the bottom of the grid

$$(\sigma_z)_a = \alpha \rho_b D_g[1 - e^{-z/(\alpha D_g)}] + (\sigma_z)_{a,t}[e^{-z/(\alpha D_g)}] \quad (12)$$

If the L/D_g ratio of the grid opening is large, Equation (12) reduces to $(\sigma_z)_a = (\sigma_z)_{a,h} = \alpha_{g,h}\rho_b D_g$. Similarly, in Figure 8*a* for zero bed depth above the top of the grid, $(\sigma_z)_a = (\sigma_z)_{a,h} = \alpha_{g,h}\rho_b D_g$. Therefore the average vertical stress exerted by the solids above the grid $(\sigma_z)_{a,t}$ multiplied by the total effective area of the grid equals the load carried by the grid minus the load carried at zero bed depth. Actually, from measurements at bed levels within the grid, $\alpha_g = 0.67$, and $e^{-L/(\alpha_g D_g)} = 0.0025$, and so a small correction to $(\sigma_z)_a$ was required. The measurements are believed to be reliable because $[d(\sigma_z)_a/\rho_b dz]_0 = 1.0$ (as is shown in Figure 20).

Concentric-cylinder-gauge Measurements

The local vertical-stress measurements used the concentric-cylinder gauge shown in Figure 9. The stresses on a controlled volume within the cylinders and the vertical forces on the solids within the volume $(\pi D_e^2/4)L$ are shown also. The principle is the same as described in the previous section. The equivalent area of the cylinders $(\pi D_e^2/4)$, divided into the difference between the load at finite and zero bed depths above the top of the cylinders, equals σ_z. In all concentric-cylinder experiments where D_a/D_p was greater than 20, $e^{-L/(\alpha D_a)}$ was negligible, and so the vertical stress transmitted through the cylinders was $\alpha_h \rho_b D_a$, by Equations (5) and (12), at zero and finite-bed depths above the cylinders. Therefore, all the vertical force exerted at the top of cylinders was exerted as additional shear stress on the tube surfaces.

The inner cylinder was suspended from a transducer which measured the load. The stationary outer cylinder absorbed its portion of the load in the annular zone plus the shear from outside the cylinders. Calibrating experiments with solids present only in the annular space between cylinders proved that the vertical shear force per unit area of surface was the same on both walls of the annular zone. These calibrating runs demonstrated also that the vertical force measured by the transducer in the actual concentric-cylinder runs was exerted over an area based on the geometric mean of the inner and outer cylinder diameters D_e. The following evidence demonstrated the validity of the concentric-cylinders measurements: (1) separate measurements of the loads on each cylinder were equal to those predicted from the geometry; (2) ρ_b equaled $\pi D_e^2/4$ divided into the maximum slope of the load-vs.-bed-depth curve at bed levels within the cylinders; and (3) $(\partial\sigma_z/\rho_b\,\partial z)_0 = 1.0$, at bed levels slightly above the cylinders, at 0 to 0.5 fractional radius (Figures 15 to 17). The point of application of the mean stress was calculated by graphical integration. With cylinders located at $r = 0$, the mean stress was exerted at $\frac{1}{3}D_e$. All σ_z data were plotted at the point of mean stress.

Thirteen cylinder arrangements were investigated. The best results were obtained with cylinders of 0.913- and 0.478-in. equivalent diameters. At cylinder-to-particle-diameter ratios below 20 erroneously high σ_z data were obtained.

Induced-shear-gauge Measurements

Radial stress σ_r was measured indirectly as a vertical shear force on a thin vertical plate suspended in a tangential plane from a transducer. The force per unit surface area of the plate equals the induced shear stress $(\tau_{rz})_i$, and $\sigma_r = (\tau_{rz})_i/\mu'$. However, $(\tau_{rz})_i \neq \tau_{rz}$, because the force on the plate can result from only a normal stress. Tangential stress σ_θ was measured from the induced force on a radial plane. The friction coefficient was taken from wall-forces-gauge measurements in the 3.8-in. tubing.

Reliable data were obtained with 0.0024-in. Sandvik stainless and 0.0033-in. spring steel plates. Figure 10 is a plot of the plate load as a function of width and length, at $r = 0$ and $z/D_t > 6$. It is apparent that the load caused by the disruption of flow around the top of the plate is appreciable. This effect was eliminated by use of data from plates of different plate lengths. Then $(\tau_{rz})_i$ equals the increment in load divided by the increment in total area (for both sides) of the plates. For plates $\frac{1}{4}$ in. or narrower $(\tau_{rz})_i$ is virtually independent of width as shown by a cross plot of $(\tau_{rz})_i$ vs. width.

Traverses of the bed were made with $\frac{1}{4}$- by $\frac{1}{8}$- by 0.0024-in. and $\frac{1}{4}$- by 1- by 0.0024-in. plates. The incremental load/(μ') (incremental area = 7/16 sq. in.) = σ_r. The bed depth z was the distance from the free surface to the centroid of the lower $\frac{7}{8}$ of the larger plate, or the portion covered by solids. However, z was obtained by graphical integration in the regions where the σ_r-vs.-z curve was not linear. The accuracy of the induced-shear measurements was shown by the constant values of σ_r in the center of the bed [as predicted by Equation (21) theory] and by a comparison of the extrapolated values of σ_r at the wall with $(\sigma_r)_w$ from wall-forces-gauge data (Figures 18 and 19).

Traverses were made in the 11.6-in. pipe with $\frac{1}{2}$- by 1- by 0.0024-in. spring steel and $\frac{1}{2}$- by 1- by 0.021-in. galvanized plates. The loads were divided by $\mu' = 0.28$ and $\mu' = 0.39$, respectively, and the results were extrapolated to zero plate thickness. Thus the method of determining σ_r in the 11.6-in. pipe is not the same as that used in the 4-in. equipment, but both techniques appear to be reliable.

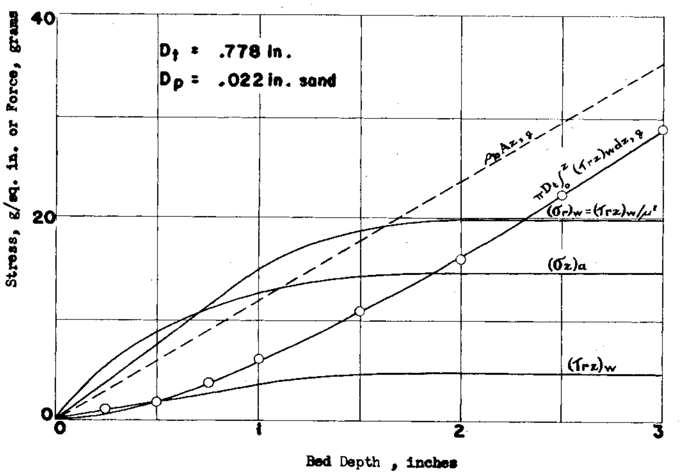

Fig. 7. Total-load-gauge measurements.

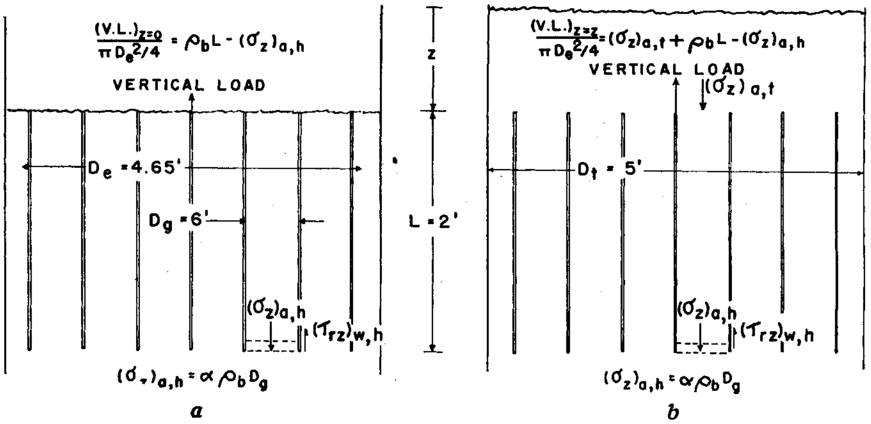

Fig. 8. Average-vertical-stress measurements: *a*, zero bed depth above grid; *b*, finite bed depth.

PROPERTIES OF SOLIDS SYSTEMS

The density or void fraction and the coefficients of friction were measured under flowing conditions. These properties depend on the particle and tube characteristics. A few static experiments were performed to develop methods for predicting the flowing-solids properties of unknown systems from static measurements.

Density and Void Fraction

The bulk density equals the particle density multiplied by one minus the void fraction. The flowing bulk density was determined by weighing the solids between two horizontal planes in the 3.8-in.

tubing after equilibrium flow conditions had been established. The same value of ρ_b was obtained from the weight of solids collected, divided by the change in bed volume during the same time interval. The particle- and flowing-bulk-density data are given in Table 2. The static loose and machine-packed bulk densities were measured also. The average density across a cross section ρ_b was found to be independent of bed depth, velocity (over a range of 0.001 to 0.9 ft./sec.), tube roughness, and tube diameter (D_t = 0.5–11.6 in.), unless the D_t/D_p ratio was less than about 20. By comparison, it can be shown from Adams' data (*1*) that the densities in an orifice and upstream are substantially equal, even though the velocities differ by a factor of 30.

The void-fraction data are presented in Figure 11. The void fraction ϵ was constant at a value of 0.39 for spherical particles and varied inversely with D_p for sand, because the small irregularly shaped particles were more difficult to compact. For irregularly shaped materials Figure 11 indicates that ϵ should be taken as 0.02 less than the static loose-packed void fraction. The data for bead catalyst indicate that a wide range of particle size decreases ϵ by about 0.02. The radial variation of ϵ was not measured. The data for static systems (*10, 11, 13, 18*) show that the high voidage necessitated by the presence of the wall exists for only a few particle diameters and has a negligible effect on the average value of ρ_b at D_t/D_p ratios greater than 20/1. However, in flowing systems shear occurs in the outer portion of the bed. The voidage is undoubtedly equal to or less than the loose-packed density in this region and is equal to the packed density in the central core. This would account for the higher flowing voidage of irregularly shaped particles compared with spheres.

Coefficients of Friction

Two coefficients are of interest: μ', the friction coefficient on the container, and μ, the coefficient of solids on solids. Both vary with the voidage (*15, 16*). In the outer region of a flowing bed, where solids-on-solids shear occurs, both the local voidage and μ should be the same as in conventional static tests where solids shearing is made to occur. Only static experiments to determine μ were carried out. Values of μ' were calculated from wall-forces-gauge measurements. These data are presented in Table 3. They were used in all calculations where a value of μ' was required. Table 3 shows that μ' is substantially independent of D_p but increases with the pipe roughness and solids roughness and/or irregularity of shape. Finally it was found that μ' was independent of the velocity of shear and the air humidity.

Because bead catalyst and sand apparently have the same value of μ' even though the shapes and sizes differ, it is believed that the values of μ' in Table 3 can be used for systems with similar surface characteristics. However, for unknown systems μ' may be predicted from static experiments. The values of μ_h' from flowing experiments (Table 3) were found to be about 80% of these measured by shearing solids over metal surfaces of comparable characteristics in essentially static tests [inclined-shear, horizontal-shear, annular-torsional-ring, and conventional shear-box (*15, 16*) experiments]. Thus $\mu_h' = 0.8\mu'_{static}$ approximately, where μ'_{static} is measured by inclined-shear tests or estimated from Figure 12, if only angle-of-repose data are available. Figure 12 was calculated from the data of Rausch (*10*). This is a plot of μ'_{static}/μ_{free} from inclined-shear experiments, where μ_{free} is the tangent of the angle of incline at which a free surface of solids starts to slide. Friction-coefficient data from inclined-shear tests are reported to show the relative values of the various coefficients from static experiments.

TABLE 3. WALL-FORCES-GAUGE TERMINAL DATA

Material	D_p, in.	μ_0'	α_0	$k_{a,0}$	μ_h'	α_h	$k_{a,h}$
3.806-in.-diam. smooth steel tubing							
Sand	0.029	0.34	0.80	0.90	0.28	0.54	1.63
	0.022	0.35	0.71	1.01	0.25	0.52	1.93
	0.015	0.38	0.63	1.06	0.28	0.56	1.59
	0.012	0.28–0.38	0.52–0.72	1.27	0.28	0.52	1.74
	0.009			1.30	0.23		
Glass beads	0.028	0.19	0.92	1.40	0.17	0.73	2.00
	0.0185	0.24–0.30	0.73–0.93	1.13	0.17	0.70	2.21
	0.011				0.14		
Bead catalyst	0.125	0.5	0.56	1.01	0.28	0.50	1.72
4.026-in.-diam. commercial pipe (rough)							
Sand	0.022				0.35	0.43	1.67

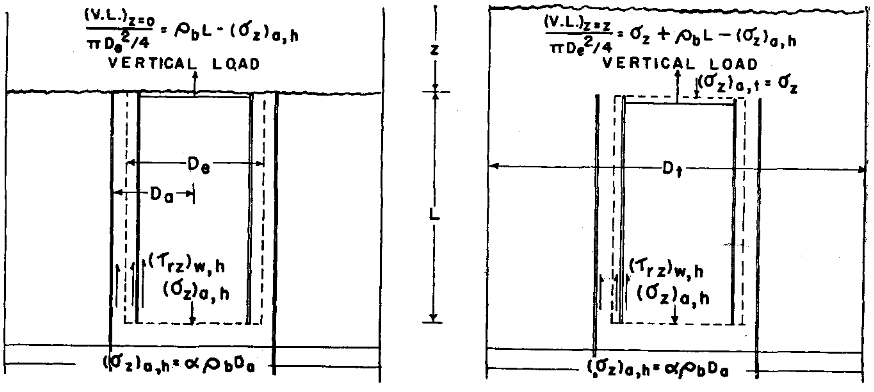

a *b*

Fig. 9. Concentric-cylinder measurements: *a*, zero bed depth above cylinders; *b*, finite bed depth.

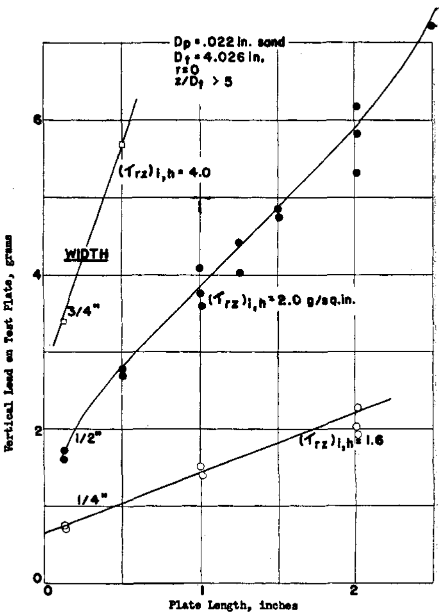

Fig. 10. Induced-shear-gauge data at center of bed.

	μ'_{static}		μ	μ_{free}
	Polished surface	Steel		
Sand	0.24	0.39	0.55	0.61
Glass bead	—	0.34		
Socony Vacuum beads	0.28	0.34		

Characteristic Properties of Flowing-solids Systems

This investigation confirmed the observations of Brinn et al. (3) of shear in approximately the outer 20% of the flowing bed and constant-velocity or rodlike flow in the remainder of the bed. The average velocity in the outer 10 to 20% of the bed was about 4% lower than the mean bed velocity, and the mean velocity was about 1% lower than the velocity in the central core. These observations are valid, however, only if the tube-to-particle-diameter ratio is greater than about 15 to 20.

The study further showed that all stresses, as well as ρ_b and μ', were independent of the rate of flow over the range of velocities studied. This would appear to indicate that motion introduces no new types of stress in solids systems and that the mechanism of stress distribution is entirely by particle-to-particle friction. There was neither tangential nor swirling motion nor torsional force in the systems studied.

All stresses vary appreciably with time, and vibration is present in all runs. Figure 13 is a photograph of the recorded variation of σ_z with time in a typical experiment. The vibration and variation of stress with time are believed to be caused by the characteristic stick-slip action described by Bowden and Tabor (2). This phenomenon occurs at the walls, in the region where shear occurs, and at the measuring-gauge surface. The percentage of variation of stress decreases as μ', D_t/D_p, and z/D_p increase.

PRESENTATION AND DISCUSSION OF STRESS DATA

In this section these data are discussed in detail. First the ratios of boundary and average stresses are presented; then the local values of stress and stress ratios are considered. The former are used in a later section to develop generalized equations for the boundary and average stresses, and the latter to develop equations for the local stresses and to explain the flowing-bed phenomena.

TABLE 4. TOTAL LOAD MEASUREMENTS

Single-cylinder measurements: D_t = 1.053 in.								
Material	D_p, in.			α_0	$k_{a,0}$	μ_h'	α_h	$k_{a,h}$
Sand	0.022			1.1	0.8	*	0.6	1.6
Concentric-cylinder measurements: bed level within cylinders								
Material	D_p, in.	D_a, in.	D_0, in.					
Sand	0.029	0.53	0.913			*	0.62	1.5
	0.022	0.53	0.913			*	0.69	1.3
	0.015	0.53	0.913			*	0.67	1.3
	0.012	0.53	0.913			*	0.43	2.1
	0.009	0.53	0.913			*	0.54	2.0
Glass beads	0.0185	0.40	0.547			*	0.9	1.6
	0.0185	0.40	0.633			*	1.0	1.5
	0.0185	0.53	0.726			*	0.9	1.6
	0.0185	0.53	0.913			*	1.5	1.0
	0.011	0.40	0.547			*	0.5	3.5

*μ' assumed from Table 3.

Stress Ratio k_a, $(\sigma_r)_w/(\sigma_z)_a$

The ratio k_a varies with bed depth and is relatively independent of D_p, $D_t(D_t/D_p > 20)$, solids material, and pipe surface. The effect of bed depth on k_a is shown in Tables 3 and 4. At zero and high bed depths, respectively, k_a is approximately 1.0 and 1.8. It must be 1.0 or less at low bed depths because free solids cannot exert a greater force than that caused by their weight, and $(\sigma_z)_a = \rho_b z$. The data indicate that k_a is about 1.4 at $(\sigma_z)_a/(\sigma_z)_{a,h} = 0.5$ and that the following equation is a fair representation of the experimental results:

$$k_a = 1.0 + 0.8\,\frac{(\sigma_z)_a}{(\sigma_z)_{a,h}} \qquad (13)$$

No uniform effect of D_p on k_a can be seen from Tables 3 and 4 at either low or high bed depths. This ratio is the same for 0.012- to 0.029-in. sands and 0.125-in. bead catalyst. Similarly, no uniform effect of D_t on k_a is noted over the range of 1 to 60 in. except at D_t/D_p ratios below 15, where k_a is considerably less than 1.0 at all bed depths. There must be no effect of D_t on $k_{a,0}$ because $(\sigma_r)_{w,0}$ is the equivalent to that produced by free solids acting on a flat plate, and $(\sigma_z)_a = \rho_b z$. The average value of $k_{a,h}$ is 1.6 to 1.8 for the small cylinders in Table 4, 1.8 for the 3.8- and 4.0-in. tubing and pipe in Table 3, and 1.45 from grid measurements in the brick-lined 60-in. vessel. The latter value was calculated from $(\sigma_z)_a$ measurements by estimating μ' for catalyst on brick from static measurements.

For sand, bead catalyst, and glass beads k_a is substantially the same. The higher values of k_a for glass beads in Table 3 are offset by the lower values in Table 4. Table 3 shows that $k_{a,h}$ is about 1.7 for sand in both smooth tubing and rough pipe, and $k_{a,h}$ in the brick-lined vessel is in the same order of magnitude.

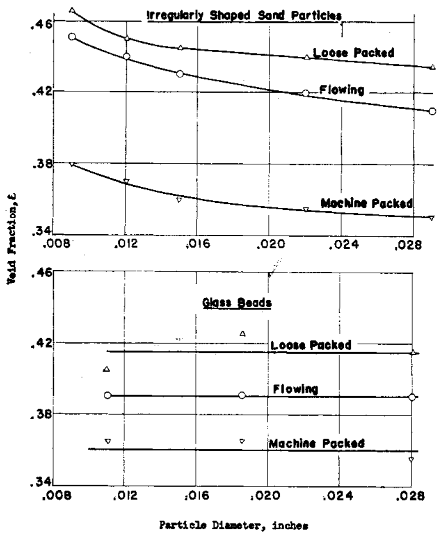

Fig. 11. Flowing- and static-void-fraction data.

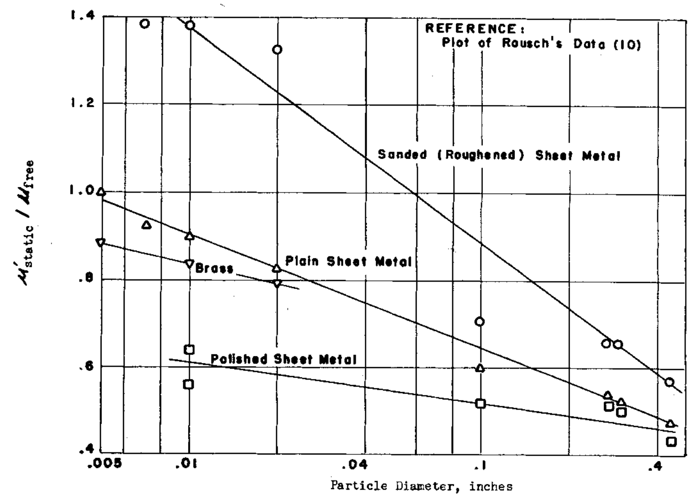

Fig. 12. Relationship between friction coefficients.

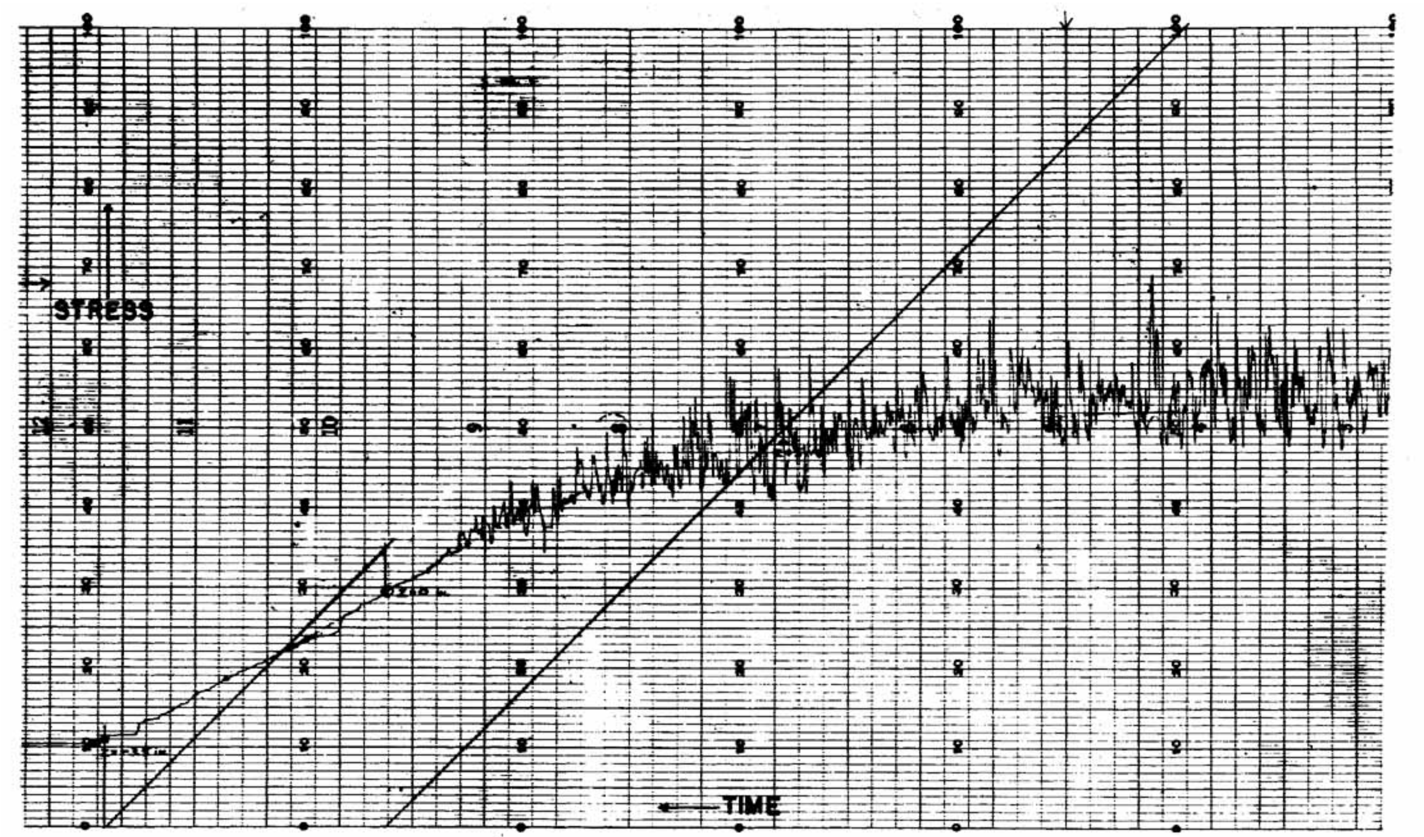

Fig. 13. Variation of vertical stress with time.

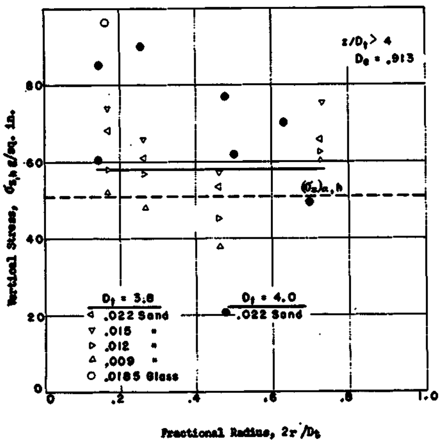

Fig. 14. Radial traverse of vertical stress at high bed depth.

Stress Ratio μ', $(\tau_{rz})_w/(\sigma_r)_w$

Table 3 indicates that μ_0'/μ_h' is approximately 1.2, and the decrease of μ' with z or $(\sigma_z)_a/(\sigma_z)_{a,h}$ is fairly rapid. The lowest value of μ' occurs at the highest normal (radial) stress, which is consistent with data for static systems (*15, 16*). Because μ'_{static} is about 20% higher than μ_h', it is suggested that the static condition is equivalent to that at zero bed depth. Table 3 shows that μ' is relatively independent of the D_t/D_p ratio ($D_t/D_p > 20$). This effect on μ' was discussed in the section on solids properties. Because the particles are actually shearing over a flat plate, μ' should be independent of D_t/D_p.

Stress Ratio α, $(\sigma_z)_a/(4)(\tau_{rz})_w$

Within the limits of accuracy of the experimental data, $k_a\mu'$, as well as k_a, varies linearly with $(\sigma_z)_a/(\sigma_z)_{a,h}$. From Equation (13) and the relationship $\mu_0'/\mu_h' = 1.2$, this linear relationship becomes

$$\frac{1}{4\alpha} = k_a\mu'$$

$$= \mu_h'\left[1.2 + 0.6\,\frac{(\sigma_z)_a}{(\sigma_z)_{a,h}}\right] \quad (14)$$

The experimental and calculated values for α are listed below:

Material	μ_h'	α_0, exp.	α_0, Eq. (14)	α_h, exp.	α_h, Eq. (14)
Sand	0.28	0.7	0.74	0.55	0.5
Glass beads	0.17	0.9	1.2	0.7	0.8
Bead catalyst	0.28	0.56	0.74	0.5	0.5
Sand (rough pipe)	0.35	—	—	0.43	0.4

This agreement with Equation (14) is good, considering that Equations (13) and (14) involve no parameters other than μ_h'.

Vertical Stress, σ_z

Although the vertical stress data are less consistent than the other measurements, they indicate that $\sigma_{z,h}$ increases with decreasing friction coefficient, is independent of D_p and probably tube roughness, and is relatively constant in the center of the bed at a value higher than the average vertical stress, $(\sigma_z)_{a,h}$. No uniform effect on $\sigma_{z,h}$ of the fractional radius over the range $2r/D_t = 0.17$ to 0.74 can be seen from Figures 14 or 15. The average of the $\sigma_{z,h}$ values for sands from Figure 14 is 58, compared with $(\sigma_z)_{a,h} = 51$. The glass beads behave similarly. This indicates that $\sigma_{z,h}$ must be lower than $(\sigma_z)_{a,h}$ in the outer portion of the bed. The data for smaller cylinders in Figure 16 show σ_z is lower at a fractional radius of 0.8 than at 0.5.

The slightly higher values of $\sigma_{z,h}$ for the larger particles in Figure 14 may result from a greater disruption of the flow pattern of the larger particles past the cylinders. Table 3 shows no such effect of D_p on $(\sigma_z)_{a,h}$. In any event this effect of D_p is small. The vertical stress for glass beads was 20 to 40% higher than for the sands in both the $\sigma_{z,h}$ and $(\sigma_z)_{a,h}$ experiments. This can be accounted for by the lower friction coefficients of glass beads. Figure 14 shows that $\sigma_{z,h}$ is slightly higher for rough pipe than for smooth tubing, but this does not appear to be consistent with the $(\sigma_z)_{a,h}$ data.

Figures 15 and 16 show the σ_z-vs.-z relationships at several radial positions. The initial gradient $(\partial\sigma_z/\rho_b\partial z)_0$ equals 1.0, 1.0, 0.5 and 0.5 at fractional radii of 0, 0.5, 0.74, and 0.8, respectively. Furthermore these gradients are constant in the outer portions of the bed from $z/D_t = 0$ to 1.0. This indicates high shear stress in this region. The distance required to transmit this shear to the center of the bed appears to be a function of the number of particle diameters of bed depth. Figure 17 shows the bed height required to reduce the vertical stress divided by $\rho_b z$ to a value of 0.75 near the center of the bed. The constancy of the z/D_p ratio at this point is shown below:

Materials	z/D_p for $\sigma_z = 0.75\rho_b z$
Sands (D_p = 0.009, 0.012, 0.015, 0.022, 0.029)	110, 100, 115, 140, 130
Glass beads (D_p = 0.011, 0.0185, 0.029)	90, 210, 150

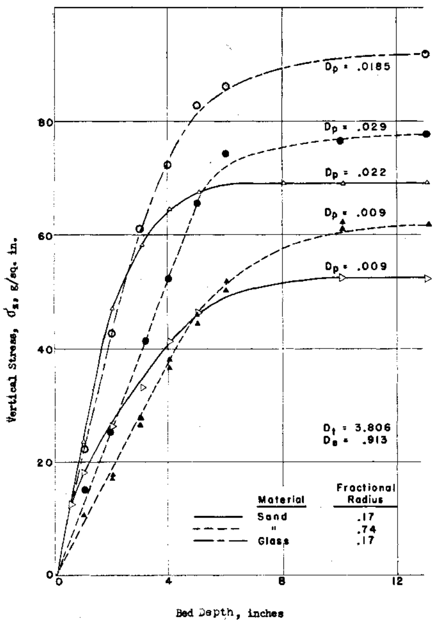

Fig. 15. Effect of bed depth on vertical stress.

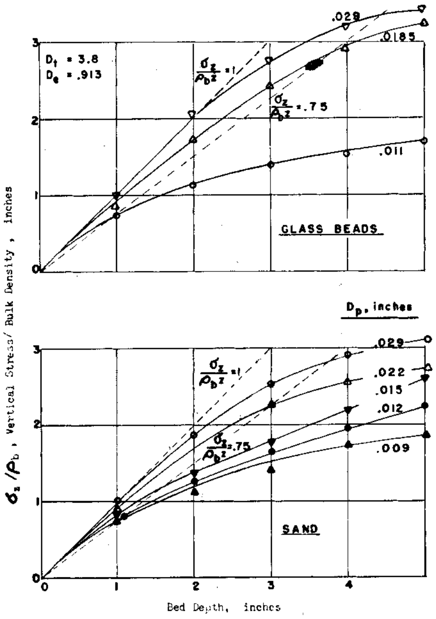

Fig. 17. Vertical stress at low bed depth.

Radial Stress, σ_r

The induced-shear data presented in Figures 18 and 19 show that σ_r is constant in the center portion of the bed and increases rapidly in the region where shear is occurring, from a fractional radius of 0.8 to 1.0, at a slope $(\partial\sigma_r/\rho_b\partial_r)_h \geqq 5$. At the axis of the pipe $(\sigma_r)_h$ equals $0.06\rho_b D_t$ and $0.09\rho_b D_t$ for the 4.0- and 11.63-in. pipes, respectively. The $(\sigma_r)_w$ data are plotted in Figures 18 and 19 for comparison.

Figure 19 is a dimensionless plot of $\sigma_r/\rho_b D_t$ vs. z/D_t, so that the data for both pipes may be compared. The agreement is satisfactory considering the different types of traverses made. The initial gradient $(\partial\sigma_r/\rho_b\partial z)_0$ is approximately equal to 1.0 at all fractional radii and even at the wall, as indicated by Table 3. At intermediate bed depths, σ_r was lower at r = 0.5 and 0.7 than at the axis of the pipe.

Tangential Stress, σ_θ

Both σ_θ and σ_r data are included in Figure 18. The difference between these stresses appears to be negligible. It is concluded that the horizontal normal stresses on radial and tangential planes are equal and that horizontal stress is exerted

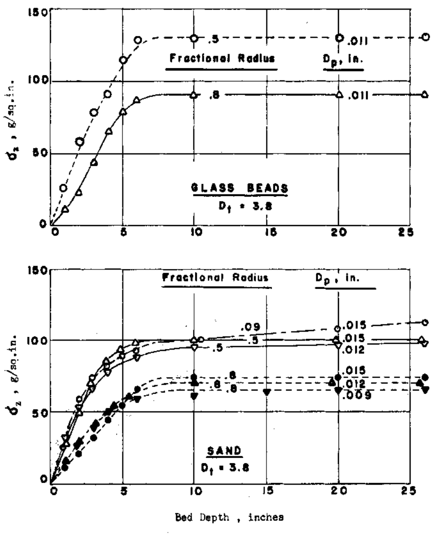

Fig. 16. Vertical stress traverse with small cylinders.

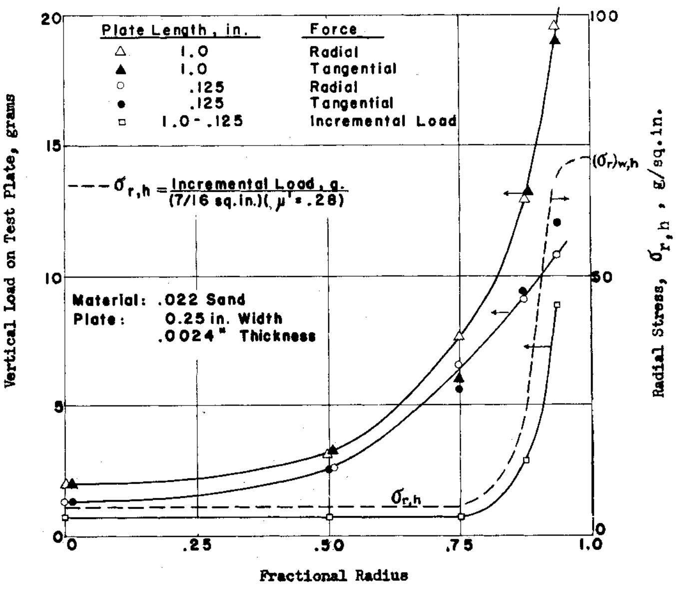

Fig. 18. Radial stress traverse at high bed depth.

equally in all directions at any given bed depth. This was further demonstrated by measuring the force normal to vertical planes inclined at various angles from a radial plane.

Stress Ratio k, σ_r/σ_z

The ratio k appears to be independent of radial position from a fractional radius of 0 to 0.7. In this region $k = (\partial\sigma_r/\rho_b\partial z)_0 = 1.0$ at low bed depths and k equals 0.1 to 0.15 at high bed depths. In the outer portion of the bed at high bed depths, k is large and equals 2 or more at the wall.

Internal Shear Stresses and Stress Ratios

The local shear stresses were not measured; however, equations will be developed in the next section which permit calculation of the shear stresses and the shear-stress ratio $\tau_{rz}/\sigma_r = \mu$.

ANALYSIS OF STRESS RELATIONSHIPS

Boundary and Average-stress Relationships

Because the solid particles flow without vertical acceleration, Equation (5) is valid for flowing systems. It can be integrated by using the relationship for k_a and μ' given by Equation (14). Substitution of Equations (7) and (14) in Equation (5) and integration from the free surface to a finite bed depth yields

$$\frac{(\sigma_z)_a}{(\sigma_z)_{a,h}} = \frac{(\sigma_z)_a}{\rho_b D_t/(4)(1.8)(\mu_h')} = \frac{1 - e^{-9.6\mu_h' z/D_t}}{1 + \frac{1}{3}(e^{-9.6\mu_h' z/D_t})} \quad (15)$$

The values of the boundary stresses can be calculated from Equations (13), (14), and (15). Thus when

$$\frac{(\sigma_z)_a}{(\sigma_z)_{a,h}} = Q$$

$$\frac{(\tau_{rz})_w}{(\tau_{rz})_{w,h}} = \frac{(\tau_{rz})_w}{\rho_b D_t/4} = \left(\frac{1.2 + 0.6Q}{1.8}\right)Q \quad (16)$$

$$\frac{(\sigma_r)_w}{(\sigma_r)_{w,h}} = \frac{(\sigma_r)_w}{\rho_b D_t/(4\mu_h')} = \left(\frac{1.0 + 0.8Q}{1.8}\right)Q \quad (17)$$

A similar relationship can be developed from the general Equation (18) for the variation of $k_a\mu'$ with Q rather than the specific Equation (14).

$$\frac{1}{4\alpha} = k_a\mu' = \mu_h'(B + CQ) \quad (18)$$

The final equation, comparable to the specific Equation (15), is

$$Q = \frac{1 - e^{-4\mu_h'(B+2C)z/D_t}}{1 + \left(\frac{C}{B + C}\right)e^{-4\mu_h'(B+2C)z/D_t}} \quad (19)$$

However B and C are constants which must be evaluated experimentally. To compare the average-vertical-stress data for different solids and vessels, $(\sigma_z)_a/\rho_b$ and bed depth were divided by $D_t/4\mu_h'$ and plotted in Figure 20. Equation (15) indicates that the data should fall on a single curve, having an initial slope of 1.0 and a maximum equal to the value of $1/k_{a,h}$. The discrepancies result from the difference between the measured value of $k_{a,h}$ and 1.8. The correlation could be improved by plotting $(\sigma_z)_a/(\sigma_z)_{a,h}$ as the ordinate, but this procedure does not permit prediction of $(\sigma_z)_{a,h}$. However, this method can be used to demonstrate the relationships between these stresses, as well as the accuracy of Equations (15) to (17). The fraction of the maximum shear and radial wall stresses, at $(\sigma_z)_a/(\sigma_z)_{a,h} = 0.5$, and the corresponding bed depth are given in the following table:

Material	$\frac{(\sigma_z)_a}{(\sigma_z)_{a,h}}$	$\frac{(\tau_{rz})_w}{(\tau_{rz})_{w,h}}$	$\frac{(\sigma_r)_w}{(\sigma_r)_{w,h}}$	$\frac{z}{D_t/\mu_h'}$
Sands ($\mu_h' = 0.28$)	0.5	0.44	0.40	0.09
Glass beads ($\mu_h' = 0.17$)	0.5	0.47	0.32	0.07
Bead catalyst ($\mu_h' = 0.28$)	0.5	0.48	0.42	0.12
Average	0.5	0.46	0.38	0.09
Calculated from Equations (15) to (17)	0.5	0.42	0.39	0.09

These equations are not valid at D_t/D_p ratios below about 15 because k_a is considerably less than 1 at all bed depths.

Local Stress Differential Equations

The experimental stress data can be employed to make Equations (1) to (3) useful for the study of solids flow. Because there is no linear acceleration in either the vertical or tangential direction, Equations (1) and (3) are valid in flowing systems. Equation (3) can be eliminated because all terms equal zero: σ_θ does not vary with θ, and all shear stresses in the tangential direction or resulting from a tangential force are zero. Because $\tau_{\theta z} = 0$, Equation (1) reduces to

$$\frac{\partial\sigma_z}{\partial z} + \frac{\partial\tau_{rz}}{\partial r} = \rho_b - \frac{\tau_{rz}}{r} \quad (20)$$

or

$$\frac{\partial\sigma_z}{\partial z} + \frac{\partial(r\tau_{rz})}{r\,\partial r} = \rho_b \quad (20)$$

In the central core of the bed (approximately 80%) there is no radial movement or acceleration and no rotation or angular acceleration. Therefore, in this region Equation (2) is valid and also $\tau_{zr} = \tau_{rz}$. Furthermore, the data show that $\sigma_\theta - \sigma_r$ equals zero. Hence

$$\left(\frac{\partial\sigma_r}{\partial r} + \frac{\partial\tau_{rz}}{\partial z}\right)_{core} = 0 \quad (21)$$

As discussed previously, at z/D_t ratios greater than about 5 all stresses including shear stresses are independent of z. Therefore, Equation (21) shows that $(\sigma_r)_{h,core}$ is independent of the radial position and is equal to $(\sigma_r)_{h,(r=0)}$. The radial stress data in the central core at high bed depths verify this deduction and hence indicate the validity of Equation (21).

In the outer portion of the bed the data show that $(\partial\sigma_r/\rho_b\partial_r)_h$ is equal to or greater than 5, rather than 0, as predicted by Equation (21). For there to be no radial acceleration in the outer section $(\partial\tau_{zr}/\rho_b\partial z)_h \leqq -5$, and τ_{zr} would reach impossibly high negative values at even moderate bed depths. It must be concluded that in the outer section of the bed there is a net transport of momentum in the radial direction by radial movement of particles. The equation in this region is

$$\left(\frac{\partial\sigma_r}{\partial r} + \frac{\partial\tau_{zr}}{\partial z}\right)_{outer\ section} = \frac{\text{radial acceleration force}}{\text{unit volume of solids}} \quad (22)$$

It should be noted that τ_{zr} is not necessarily equal to τ_{rz} in the outer section because particles are free to rotate about a tangential axis in this region.

Local Stress Relationships

At high bed depths

$$\frac{\partial\sigma_z}{\partial z} = 0$$

and Equation (20) integrates to

$$(\tau_{rz})_h = \frac{\rho_b r}{2} \quad (23)$$

where the arbitrary function of integration was evaluated as zero, either from Equation (8) or at $r = 0$, where $\tau_{rz} = 0$ from symmetry. Thus $(\tau_{rz})_h$ is independent of z, as predicted. From Equa-

TYPICAL VALUES OF $\tau_{rz}/(\tau_{rz})_{w,h} = \tau_{rz}/(\rho_b D_t/4)$

Fractional radius	$z/D_t = 0.25$	0.5	1	5
0	0	0	0	0
0.25	0.007	0.11	0.205	0.25
0.5	0.015	0.22	0.41	0.50
1.0 [Equations (15), (16)]	0.55	0.8	0.9	1.0

tion (20), $(\tau_{rz})_{0,core} = 0$, because Figures 15 and 16 show that $(\partial\sigma_z/\rho_b\partial z)_0 = 1.0$ from $r = 0$ to 0.5. At intermediate bed depths over the central portion of the bed, where $\partial\sigma_z/\partial z$ is approximately constant (i.e., $\partial\sigma_z/\partial z = (d\sigma_z/dz)_{core}$ = constant),

$$(\tau_{rz})_{core} = \frac{r}{2}\left[\rho_b - \left(\frac{d\sigma_z}{dz}\right)_{core}\right] \quad (24)$$

These equations show that the (vertical) shear stress, τ_{rz}, varies linearly with the radius if, and only if, the vertical stress σ_z does not vary radially. Similarly, the necessary condition for a linear-shear-stress distribution in a comparable fluid system is that the radial velocity gradient does not vary axially (*8*).

Equations (23) and (24) give τ_{rz} at any point in the core. Typical values of the dimensionless group $\tau_{rz}/(\tau_{rz})_{w,h} = \tau_{rz}/(\rho_b D_t/4)$ calculated from Figure 15 for 0.022-in. sand are given on page 136 to show how τ_{rz} varies throughout the bed.

At intermediate depths in the central portion of the bed

$$\frac{\partial\tau_{rz}}{\partial z} = -\frac{r}{2}\left(\frac{d^2\sigma_z}{dz^2}\right)_{core}$$

from Equation (24), and from Equation (21)

$$(\sigma_r)_{core} = (\sigma_r)_{(r=0)} + \frac{r^2}{4}\left(\frac{d^2\sigma_z}{dz^2}\right)_{core} \quad (25)$$

As $d\sigma_z/dz$ is continually decreasing, the second derivative is negative and σ_r is higher at the center of the bed at intermediate bed depths. This effect was observed experimentally. At very low bed depths $(d\sigma_z/\rho_b dz)_{0,core} = 1$, $(d\tau_{rz}/\rho_b dz)_{0,core} = 0$ from Equation (24), and $\partial\sigma_r/\partial r$ is again zero.

Approximate equations for the variation of σ_z and σ_r with bed depth in the central core can be developed from a force balance around the central core up to the plane of shear ($2r/D_t = 0.75$, approximately) by substituting $k\mu$, σ_z, and $0.75D_t$ into Equation (5). The experimental data show that k varies inversely with σ_z approximately according to the equation $1/k = 1 + 9\sigma_z/\sigma_{z,h}$, but the product $k\mu$ is relatively independent of bed depth at a value of ⅓ for sands. Therefore, very approximately,

$$\left(\frac{\sigma_z}{\sigma_{z,h}}\right)_{core} = \frac{\dfrac{\sigma_z}{\rho_b D_t}}{1.8}$$

$$= 1 - e^{-1.8z/D_t} \quad (26)$$

and

$$\left(\frac{\sigma_r}{\sigma_{r,h}}\right)_{core} = \frac{\dfrac{\sigma_r}{\rho_b D_t}}{18}$$

$$= \frac{1 - e^{-1.8z/D_t}}{1 - 0.9e^{-1.8z/D_t}} \quad (27)$$

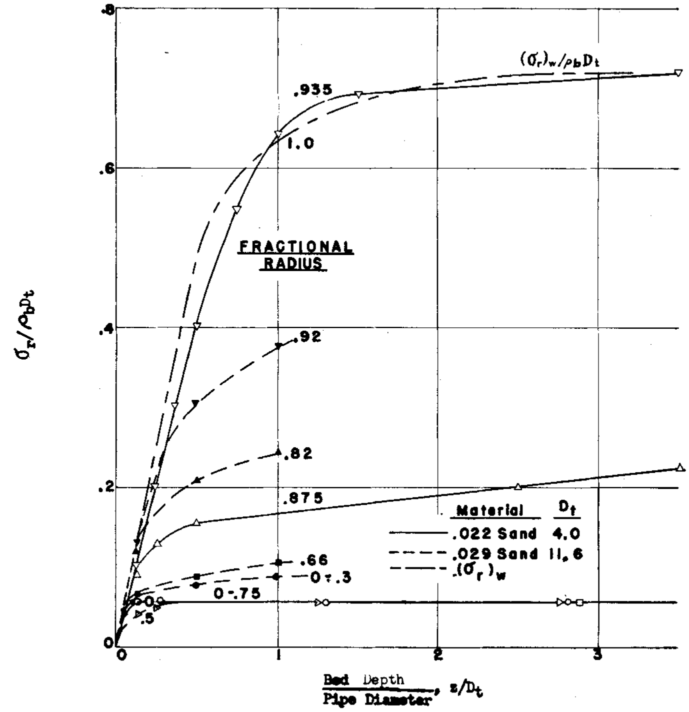

Fig. 19. Effect of bed depth and pipe diameter on radial stress.

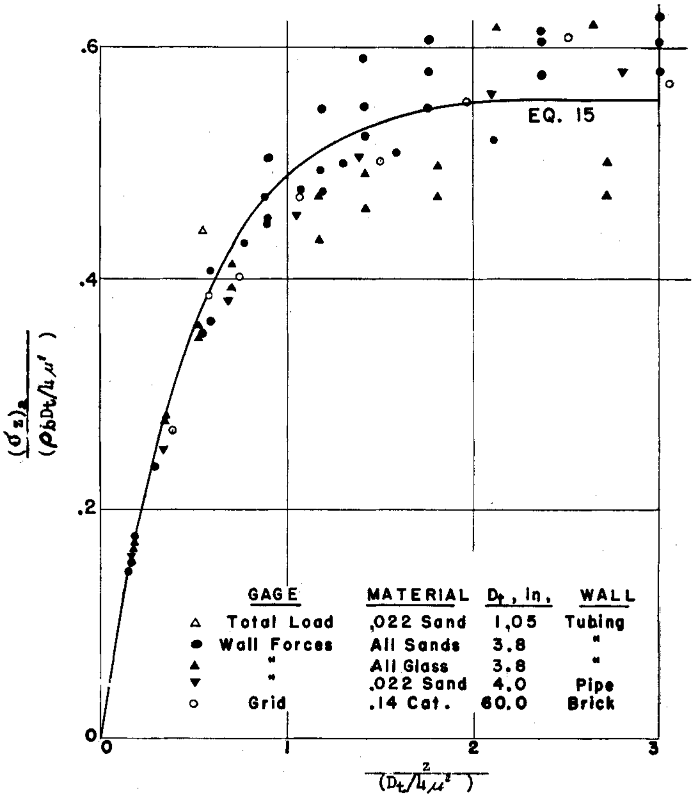

Fig. 20. Comparison of Equation (15) with experimental data.

For other materials 1.8 should be replaced by 1.8 $(\mu'_{material}/\mu'_{sand})$.

Stress Ratio μ, τ_{rz}/σ_r

The stress ratio μ equals a coefficient of friction of solids on solids only when shearing occurs at the point of measurement. The τ_{rz} and σ_r data in the central portion of the bed appear to indicate that μ increases continuously with both bed depth and fractional radius until μ_h is about two or three times as large as the fractional radius at high bed depth and a fractional radius of 0.7 or 0.8. The values of $(\tau_{rz})_{h,core}$ and $(\sigma_r)_{h,core}$ and hence their maximum ratio have not been established accurately, however. This high value of μ suggests that solids behave almost as a compact rigid body in the center of the bed, and they must either fracture or flow around each other. At a fractional radius of 0.7 to 0.8, μ equals the coefficient of friction required for this to occur, and increases in voidage, rotation, shear, and velocity gradient result. Beyond this point μ decreases rapidly to the value of about 0.5, as determined by conventional "static" friction tests, where the voidage at the shear plane is comparable. The stress ratio at the wall must decrease to μ', and therefore σ_r, which equals τ_{rz}/μ, increases with the fractional radius to the wall because $\tau_{rz}/\mu < (\tau_{rz})_w/\mu'$.

SUMMARY

In this study the local and boundary stresses in flowing beds of solids have been measured and found to be consistent with theoretical equations developed to relate these stresses, if the D_t/D_p ratio is greater than 20. Methods are presented to predict from static friction and density tests the solids properties required to evaluate the stresses in any given system.

All stresses are independent of the solids velocity and increase exponentially from zero to maximum values at bed-depth-to-particle-diameter ratios greater than about 5. The ratio of the wall radial stress to the average vertical stress increases with bed depth from 1.0 to 1.8, and μ', the wall friction coefficient, decreases about 20%. Equations are presented for calculation of the stresses and stress ratios as a function of bed depth, except in the outer portion of the bed, where solids-solids shear occurs.

The internal stresses are related to each other by the differential equations

$$\frac{\partial \sigma_z}{\partial z} + \frac{\partial (r\tau_{rz})}{r\,\partial r} = \rho_b$$

and

$$\frac{\partial \sigma_r}{\partial r} + \frac{\partial \tau_{rz}}{\partial z} = 0$$

except that the latter is not valid in the outer portion of the bed, where shear occurs and there appears to be a radial transport of momentum. In the central portion of the bed (1) the bulk density and velocity are constant; (2) the particles flow in a rodlike manner as a compact rigid body; (3) the radial-to-vertical-stress ratio k decreases with bed depth from 1.0 to about 0.1; (4) the shear stress τ_{rz} is not related to the radial stress σ_r but varies almost linearly with the fractional radius, and their ratio μ increases with both bed depth and fractional radius; and (5) the radial and vertical stresses are independent of the radial distance. The data appear to indicate that shearing occurs at the radial distance where μ_h has increased to a value greater than 2. This may be the maximum value of the coefficient of friction of solids on solids where the local density at the shear plane is high. At larger radial distances a velocity gradient is established, the voidage is increased as rotational shearing occurs, the radial stress increases rapidly with the fractional radius, and μ_h decreases to about 0.5, the friction coefficient where the voidage at the shear plane is approximately equal to that in static friction tests. At the wall $(\tau_{rz})_w/(\sigma_r)_w = \mu'$, which is considerably less than μ, and therefore σ_r increases with radial distance to the wall.

ACKNOWLEDGMENT

The author wishes to express his appreciation to C. G. Kirkbride for suggesting the problem, to J. J. Donovan for strain-gauge advice, to R. L. Pigford and J. A. Gerster for many helpful suggestions, to Sun Oil Company for permission to use the measurements in the 5-ft. kiln, and to Houdry Process Corporation for the use of the 11.63-in. equipment and for the static-density determinations.

NOTATION

Units are force, F; length, L; mass, M; and time, T.

A = area, L^2
B, C = constants
D_a = average opening diameter = one-half diameter of outer cylinder, L
D_e = equivalent diameter = geometric mean diameter of inner and outer cylinders, L
D_g = grid opening, L
D_p = particle diameter, L
D_t = tube diameter, L
g = acceleration of gravity, L/T^2
g_c = proportionality factor, ML/FT^2
k = ratio of radial stress to vertical stress = σ_r/σ_z
k_a = ratio of radial stress at wall to average vertical stress = $(\sigma_r)_w/(\sigma_z)_a$
L = length, L
Q = $(\sigma_z)_a/(\sigma_z)_{a,h}$ = fraction of maximum value of the average vertical stress
r = radial distance, L
z = vertical distance or bed depth, L
α = stress ratio $0.25\,(\sigma_z)_a/(\tau_{rz})_w = 1/(4k_a\mu')$
α_g = α within the grid
ϵ = void fraction
θ = angle, radians, or tangential direction
μ = stress ratio τ_{rz}/σ_r (= coefficient of solids friction only if shear occurs perpendicular to σ_r)
μ' = coefficient of friction of solids on pipe wall
μ_{static} = coefficient of friction of solids on metal from inclined shear tests
μ_{free} = coefficient of friction of solids on solids at a free surface = tangent of angle of repose
ρ_b = resultant body force per unit volume of solids = $[\rho_b' - (1-\epsilon)\rho_f]\,g/g_c$, F/L^3
ρ_b' = bulk density, M/L^3
ρ_f = fluid density, M/L^3
σ = normal stress acting on a perpendicular plane, F/L^2
σ_r = radial stress acting in a radial direction, F/L^2
$(\sigma_r)_w$ = radial stress at the wall, F/L^2
σ_z = vertical stress acting in a vertical direction, F/L^2
$(\sigma_z)_a$ = average vertical stress across bed at a given bed depth = $(1/A)\int_0^A \sigma_z\,dA$, F/L^2
$(\sigma_z)_{a,t}$ = average vertical stress at top of concentric cylinders, F/L^2
σ_θ = tangential stress acting in the tangential direction, F/L^2
τ = shear stress acting in a plane parallel to the stress, F/L^2
τ_{rz} = shear stress resulting from a radial force, in vertical direction, F/L^2
$(\tau_{rz})_w$ = τ_{rz} at the pipe wall, F/L^2
$(\tau_{rz})_i$ = induced shear stress on a test plate placed perpendicular to the stress being measured, F/L^2
τ_{zr} = shear stress resulting from a vertical force, in radial direction, F/L^2
$\tau_{z\theta}$ = shear stress resulting from a vertical force, in tangential direction, F/L^2
$\tau_{\theta z}$ = shear stress resulting from a tangential force, in vertical direction, F/L^2
$\tau_{r\theta}$ = shear stress resulting from a radial force, in tangential direction, F/L^2
$\tau_{\theta r}$ = shear stress resulting from a tangential force, in radial direction, F/L^2
$(d\sigma_z/dz)_{core}$ = constant value of $\partial\sigma_z/\partial z$ from $r = 0$ to $r = r$ in central core, F/L^3

Subscripts

h = value of stress at high bed depths, $z/D_t > 5$
o = value of stress at very low bed depths, $z = 0$
$(r=0)$ = value of stress at center line of bed, r = radial distance = 0
core = value of stress in central core of bed at a given bed height

Presented at A.I.Ch.E. New York Meeting